LAWRENCE
LIVERMORE
NATIONAL
LABORATORY

LLNL-PROC-645760

Evaluation of the Effect of Realistic and Synthetic Infow on the Power and Loading Pattern of Wind Turbines

H. Gopalan, D. Chandar, C. Gundling, J. Sitaraman, W. Henshaw, J. Mirocha, S. Wharton, W. Miller, J. Newman, P. Klein

November 7, 2013

AIAA SciTech
National Harbor, MD, United States
January 13, 2014 through January 17, 2014

Disclaimer

Evaluation of the effect of Realistic and Synthetic Inflow on the Power and Loading Pattern of Wind Turbine

Harish Gopalan[*], Dominic Chandar[†]
Christopher Gundling[‡], Jayanarayan Sitaraman[§]
Department of Mechanical Engineering, University of Wyoming, Laramie, WY 82071, USA

William D. Henshaw[¶], Jeffrey D. Mirocha[‖]
Sonia Wharton[**], Wayne O. Miller[††]
Lawrence Livermore National Laboratory, 7000 East Avenue, Livermore, CA 94550, USA

Jennifer Newman[‡‡], Petra Klein
School of Meteorology, The University of Oklahoma,120 David L. Boren Blvd., Norman, OK 73072, USA

Comparison of the differences between realistic and synthetic inflow models on the wind turbine power prediction and loading patterns is investigated by performing coupled mesoscale-microscale simulations. For the mesoscale part, two different frameworks are considered:(i) Weather Research and Forecasting (WRF) model framework and (ii) synthetic inflow generated using Mann's model. For the microscale part, four different CFD solvers are considered: (i) free-vortex code, (ii) Two actuator disk based large eddy simulation (LES) codes with overset capability, and (iii) full rotor based method capable of detached eddy simulation (DES). The coupling between the mesoscale and microscale codes are performed using a mesoscale microscale coupling interface (MMCI) developed as a part of our earlier work. This framework allows the efficient interpolation of data between the different codes in an automated and parallel fashion. Initial results that have been obtained from the study are included in the abstract. The final paper will encompass a detailed comparison between realistic and synthetic inflow for different turbulent intensities, shear distributions and stability conditions.

[*]Post-doctoral Research Associate, Department of Mechanical Engineering, University of Wyoming, Laramie, WY 82071, USA, Member.
[†]Post-doctoral Research Associate, Department of Mechanical Engineering, University of Wyoming, Laramie, WY 82071, USA, Member.
[‡]Graduate Student, Department of Mechanical Engineering, University of Wyoming, Laramie, WY 82071, USA, Student Member.
[§]Assistant Professor, Department of Mechanical Engineering, University of Wyoming, Laramie, WY 82071, USA, Member.
[¶]Research Staff, Centre for Applied Scientific Computing, Lawrence Livermore National Laboratory, 7000 East Avenue, Livermore, CA 94550, USA.
[‖]Technical Leader, Wind Energy Research Group, Lawrence Livermore NationalLaboratory, 7000 East Avenue, Livermore, CA 94550, USA.
[**]Research Scientist, Atmospheric, Earth and Energy Division, Lawrence LivermoreNational Laboratory, 7000 East Avenue, Livermore, CA 94550, USA.
[††]Thermal Fluids Group Leader, Lawrence Livermore National Laboratory, 7000 East Avenue, Livermore, CA 94550, USA.
[‡‡]Graduate Student, School of Meteorology, The University of Oklahoma,120 David L. Boren Blvd., Norman, OK 73072, USA.
Associate Professor, School of Meteorology, The University of Oklahoma,120 David L. Boren Blvd., Norman, OK 73072, USA.

I. Introduction

THE accurate numerical prediction of the wind turbine power production and loading is a complex multi-scale spatial and temporal problem. The flow upstream of the wind farm is determined by the local wind patterns in the atmospheric boundary layer and this can be affected by the global wind patterns. The length scale of these flow patterns are of the order of several meters/kilometers and can last for several hours. These wind patterns interact with the turbulent boundary layer developed over the surface of the turbine blades. The size of these boundary layers are of the order of few micro-meters and have a life time of few seconds. The accurate predictions of both these flow regimes are necessary to provide an efficient wind farm prediction tool. The upscaling of a micro scale code[1] (adding numerical capability to predict the atmospheric wind pattern) or downscaling of an atmospheric boundary layer code[2,3](addition of capability to predict wind turbine aerodynamics) is clearly not the optimum solution for this problem due to the multi-scale nature of the problem. It is becoming widely acknowledged that the use of coupled mesoscale microscale approaches are essential for improving the performance of a wind farm. The coupling procedure can be performed in two different ways: (i) realistic inflow and (ii) synthetic inflow. In the former approach all the scales of motions are explicitly modeled and the solvers used for the different regions of the flow are coupled together to predict the final wind farm performance. In the latter approach, empirical methods are used to approximate the inflow that the wind farm sees. The latter approach is computationally inexpensive compared to modeling all the scales in the flow. However, it is unclear how the use of artificial methods affect the numerical prediction of the turbine aerodynamics and loading under different atmospheric conditions that the wind turbine faces. For example, Park et. al[4] found that for a stable boundary later, turbine-scale variables like wind-speed, wind shear, etc. are strongly inter-related and should not be prescribed independently. However, most of the synthetic inflow generators do not currently have the capability to account for the relation between the different variables and the difference in results due to independently prescribing them is unclear.

To address this issue, the current study investigates coupled mesoscale microscale simulations using realistic and synthetic inflow. Realistic inflow is generated using the WRF-LES simulations while the synthetic inflow is generated using prescribed inflow profile superimposed with Mann fluctuations.[5] For the microscale part, four different solvers ranging from a free-wake code to a full rotor code are considered. This was done to compare the effect of the inflow condition on the wind turbine parametrization. It is expected that there will be differences in the loading pattern and the understanding of this issue would provide the wind farm designers with useful information on designing the blades for wind turbines.

The rest of the abstract is arranged as follows. The details of the different solvers and the coupling procedure is discussed in Section 2. Section 3 demonstrates the initial results from the study. Future work is presented in Section 4.

II. Computational Tools

The computational framework consists of three different parts: (i) mesoscale solver, (ii) microscale solver and (iii) coupling module. WRF model and a synthetic inflow model are used as the mesoscale solvers. Four different CFD solvers of varying complexity are considered as the microscale solvers. The coupling module, referred to as the mesoscale microscale coupling interface (MMCI) performs two functions: (i) postprocesses the velocity flow field data from mesoscale solver to provide input and initial flow field to the microscale solvers and (ii) sets up the overset grid assembly and interpolation between the CFD solvers. Brief description of the mesoscale and microscale solvers are outlined below. The details of these solvers and their validation can be found in the literature.[6–9] Detailed description of synthetic inflow and MMCI is provided here.

A. Mesoscale Solvers

1. WRF

In this work, we use version 3.3.3 of the WRF model as the mesoscale solver for performing LES of the atmospheric boundary layer (ABL). The WRF dynamical core and its surrounding software framework and physics interfaces are well suited to application of atmospheric boundary layer flows, and the modeling system has been validated for numerical weather prediction. WRF contains a number of SGS stress models for calculation of the SGS stress tensor. The current study uses the nonlinear backscatter and anisotropy (NBA) model of Kosovic[10,11] with a 1.5-order SGS turbulent kinetic energy (TKE) closure. The surface

shear stress calculations were modified to specify the roughness length z_0 explicitly in the calculations. This was necessary since the default value of the roughness length ($z_0 = 0.1m$) cannot be used for both the wind farm simulations. The surface heat flux was set to zero in all the WRF simulations while the friction velocity was calculated using the Monin-Obukhov theory. The default numerical schemes are used for spatial discretization and time marching.

2. *Synthetic Inflow Solver*

The synthetic inflow solver consists of a mean velocity profile and superimposed fluctuations. The fluctuations in the current study are generated using the algorithm developed by Mann.[5] This algorithm is based on a model of the spectral tensor and is capable of simulating all three components of a three-dimensional incompressible turbulence field. Furthermore, it can simulate turbulence with the same second order statistics as the atmosphere. The details of the model can be found in Ref.[5] The model allows the generation of anisotropic fluctuations and the ability to specify the turbulent intensity. However, the model is applicable only to neutral boundary layer. Hence, the synthetic inflow has been implemented in two different forms:

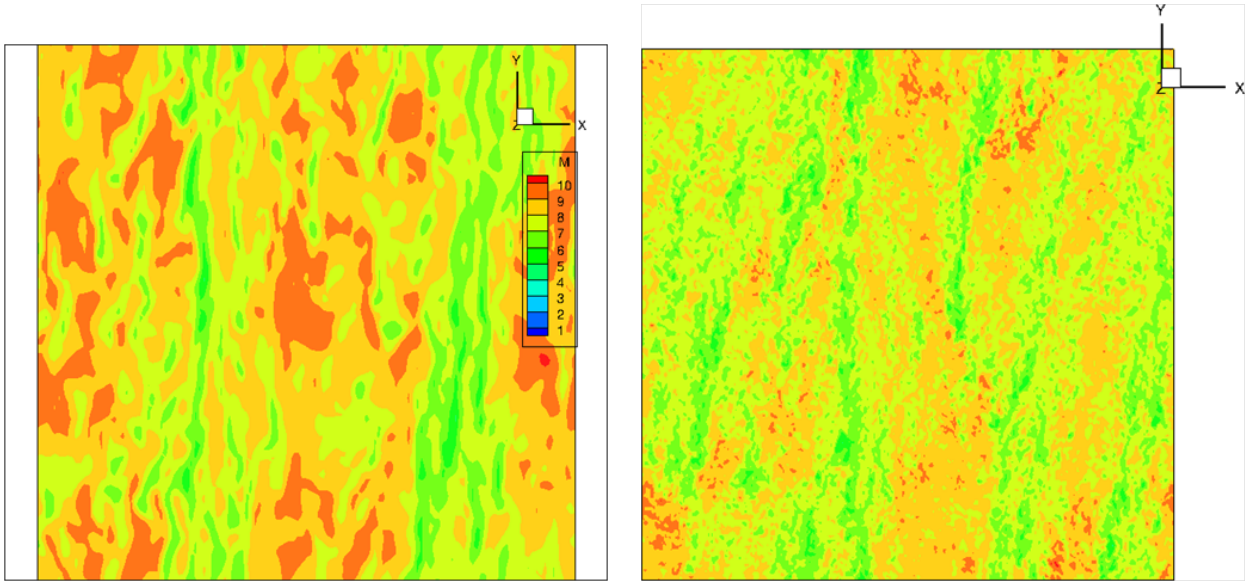

Figure 1. Comparison of the wind speed at $z = 65$ m for a neutral boundary layer on a domain size of $2048 * 2048 * 1024$ m obtained from WRF: (a) Grid resolution of $128 \times 128 \times 256$ and (b) Grid resolution of $512 \times 512 \times 512$.

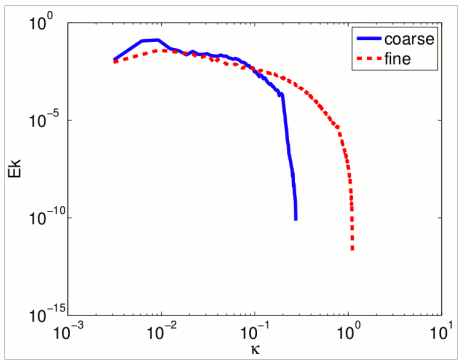

Figure 2. Comparison of the energy spectrum at $z = 65$ m for the coarse and fine grid cases in the previous figure.

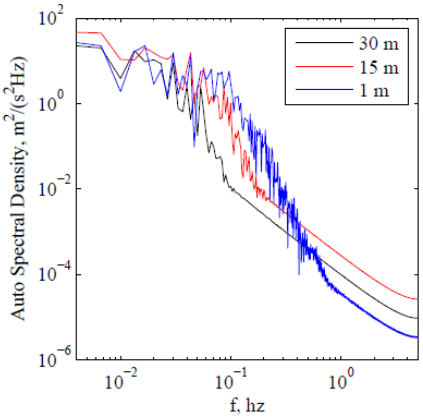

Figure 3. Comparison of the wind turbine response for a generic turbine operating in the neutral boundary layer. Inflow data was obtained from LES using OpenFOAM and aeroelastic response was studied using NREL-FAST.[12]

1. Inflow model: In this form, the flow-field is decomposed as follows

$$u_i(\vec{x},t) = U_i(\vec{x}) + u_i^{'}(\vec{x},t) \tag{1}$$

where u_i is the inflow velocity, U_i is the mean inflow velocity and $u_i^{'}$ is the fluctuations generated by the model. U_i can be specified using a log-law or power law. This form is applicable only for the neutral boundary layer.

2. Small-scale model: In this method, the flow-field is decomposed as follows

$$u_i(\vec{x},t) = U_i(\vec{x},t) + u_i^{'}(\vec{x},t) \tag{2}$$

where $U_i(\vec{x},t)$ is the inflow velocity condition from LES of the atmospheric boundary layer and $u_i^{'}(\vec{x},t)$ is the resolvable fluctuations which are generated using Mann model. To understand the need for this term, let us consider two different WRF simulations as shown in Fig 1 and the comparison of the energy spectra (see Fig 2). The portion of the energy beyond $\kappa = 0.1$ is not resolved in the coarse WRF-LES simulations. However, studies of wind turbine response (see Fig 3) showed that the small-scale structures in the atmosphere are very important from the turbine point of view and that the turbine responds dynamically to these disturbances. In particular it was observed that the small-scale structures corresponding to dx=1-3 m or $\kappa \sim 1$ have to be accurately captured for studying the structural response of the wind turbine. However, such fine scale computations of the atmospheric boundary layer are not feasible. The use of the small-scale model allows us to account for the portion of the spectrum which can be resolved by the microscale solvers and those which are not resolved in mesoscale simulations. In addition, the main advantage of the small-scale synthetic model is its independence of the atmospheric stability. Hence, for stable and convective boundary layers, WRF-LES can be performed using coarse grid resolutions and the synthetic inflow through the small-scale model can be added to account for the portion of the spectrum that is not resolved.

The ability of the small-scale model to add fluctuations over a specified range of wavenumbers is shown in Fig. 4. Figures. 4a and b show the wind speed before and after the addition of fluctuations for a FLOWYO horizontal resolution of 8 m with a WRF inflow resolution of 16 m.. It can be seen that the fluctuations have been added only at the smaller scales. To show that the method works, simulations were performed for a wind turbine blade used in the off-shore Lillgrund wind farm with turbulent inflow provides from WRF-LES simulations at $dx = 16$ m. The hub-height wind speed is shown in Fig 5. It can be seen that small-scale structures which were not resolved in the mesoscale simulations (see Fig 1a) are visible in the microscale simulations.

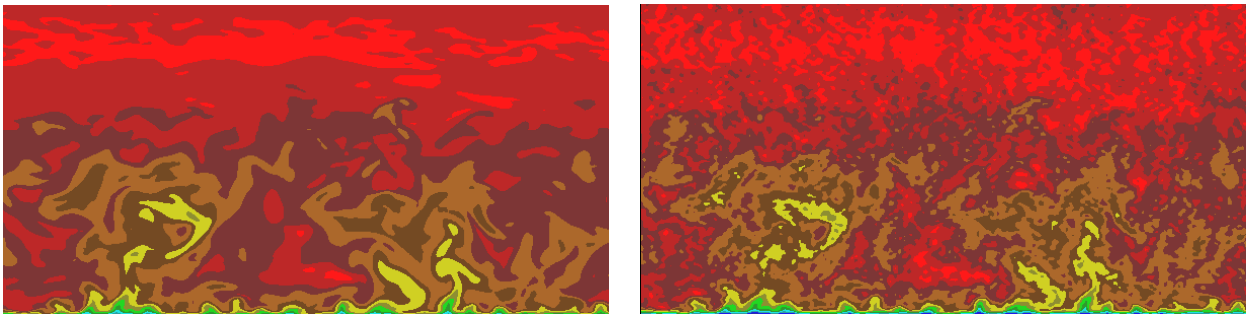

(a) (b)

Figure 4. Instantaneous wind speed along a spanwise plane to demonstrate the synthetic small-scale model: (a) No added fluctuations and (b) Fluctuations added using the small-scale model.

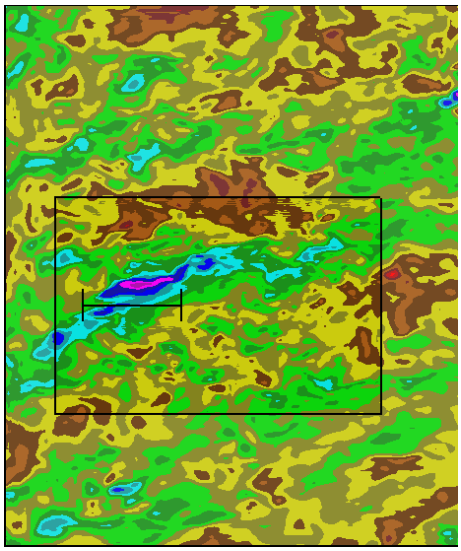

Figure 5. Wind speed at hub-height ($z = 65$ m) for turbine blade used in the Lillgrund wind farm. The inflow condition has been modified using the synthetic small-scale model.

B. Microscale CFD Solvers

Three different solvers using different levels of wind turbine parametrization are used to demonstrate the coupling approach. These solvers range from a simple free-vortex code to a full CFD code with adaptive mesh refinement. The free-vortex code can be coupled with the WRF data only in a traditional coupling manner while the other two codes can be used in both, the traditional and overset manner.

1. UWake

UWake is an in-house free-vortex wake approach that uses a Lagrangian formulation of the vorticity-transport equation to model the time evolution of vorticity fields. Considering the dominant structures in the wind turbine flow field to be the tip and root vortices, the present analysis considers a single tip and root vortex for each wind turbine blade, released from the blade tip and root respectively. The vortex elements are assumed to convect with the fluid particles. With this assumption, the governing vorticity transport equation can be expressed in Lagrangian form as

$$\frac{d\vec{r}(\psi,\zeta)}{dt} = \vec{V}(\vec{r}(\psi,\zeta)), \tag{3}$$

where $\vec{r}(\psi,\zeta)$ defines the position vector of a wake marker, located on a vortex filament that is trailed from a rotor blade located at an azimuth ψ, and was first created when the blade was located at an azimuth $(\psi-\zeta)$. The vorticity transport equation can then be written in the partial differential form as

$$\frac{d\vec{r}(\psi,\zeta)}{d\psi} + \frac{d\vec{r}(\psi,\zeta)}{d\zeta} = \frac{1}{\Omega}\vec{V}(\vec{r}(\psi,\zeta)) \tag{4}$$

The right hand side velocity accounts for the instantaneous velocity field encountered by a marker on a vortex filament in the rotor wake. This includes the free-stream velocity, the induced velocities due to the vortex filaments present in the wake, and the induced contributions of the bound circulation representing the lifting rotor blades. This equation must be discretized into a set of finite difference equations that can then be numerically integrated. The time marching algorithm is a 2nd order backward predictor corrector algorithm.[13] The velocity term in the vorticity transport equation is computed from the Biot-Savart law:

$$\vec{V}(\vec{r}) = \frac{\Gamma}{4\pi}\frac{h^2}{\sqrt{h^2+r_c^2}}\int \frac{\vec{dl}\times\vec{dr}}{|\vec{r}|^3}, \tag{5}$$

where $\vec{V}(\vec{r})$ is the velocity induced at a point P located at $\vec{r}$ relative to the vortex element $\vec{dl}$. The integral is evaluated over the entire length of the vortex filament. Γ is the total strength of the filament, and $\vec{dl}$ is an elemental unit vector along the vortex filament. The circulation released at the blade tip is assumed to be equal to the maximum bound circulation along the outboard half of the blade and the circulation at the root is the negative of the maximum circulation in conformance with Helmholtz laws. The tip and root vortex core radius is noted r_c, and h is the perpendicular distance of the evaluation point from the influencing vortex element. An appropriate aerodynamic model for the blade has to be coupled with a free-vortex wake model to predict both the wake evolution as well as the blade loading. UWake utilizes a blade element model for the aerodynamic modeling, with aerodynamic coefficients interpolated from tabulated 2-D airfoil data. In addition, the Du-Selig[14] stall-delay model is included to account for the aerodynamics at separated flow conditions.

2. Flowyo

Flowyo is an in-house compressible mixed finite volume/difference code that solves the strong conservative form of the filtered Navier-Stokes equations. The spatial discretization of the derivatives are performed either using a third-order Monotone Upstream-centered Schemes for Conservation Laws (MUSCL) scheme[15] or a fifth-order WENO scheme[16] or a blended fourth-order central scheme. Temporal discretization is accomplished using a second-order implicit backward difference scheme. To reduce the storage associated with the use of the exact Jacobians, a LU-SGS scheme[17] is used for the solution of the implicit system. The SGS stress closure can be achieved using Smagorinsky model,[18] 1.5-order SGS TKE closure,[19] wall-adapting local eddy viscosity model,[20] detached eddy simulation[21] or delayed detached eddy simulation.[22] The Smagorinky and 1.5-order SGS TKE closure also have an option for using the non-linear SGS stress

tensor of Kosovic.[10] The wind turbine can be parametrized using an actuator disc or line model in this solver. Part of the overset grid assembly module is in-built in Flowyo.

3. Cgins

Cgins is an open-source incompressible flow solver that is continuously developed by Lawrence Livermore National Lab as a part of the open-source overture framework, an object-oriented numerical tool for solving partial differential equations. The spatial discretization can be performed using second or fourth order schemes. A number of implicit time marching methods are available for temporal discretization. Pressure velocity coupling is achieved using predictor corrector methods. The algebraic system for pressure and velocity can be solved using multigrid or Petsc solvers. The SGS stress closure can be achieved using an implicit-LES method. The wind turbine can be parametrized using an actuator disc in this solver. The coupling of Cgins with MMCI is currently under development.

4. HELIOS

Helicopter Overset Simulation Tool (HELIOS), is a software framework targeted towards prediction of vortex dominated flows seen in rotary-wing systems. HELIOS is co-developed by the U.S Army and the University of Wyoming. In contrast to traditional CFD codes which are built on a single gridding paradigm, (e.g. structured, unstructured or Cartesian grids) HELIOS relies on a more flexible multi-mesh approach. Body conforming structured or unstructured grids are used for representation of the wetted surfaces, while Cartesian grids capable of automatic solution based adaptation are used away from the body. The multi-mesh approach is implemented using a multiple solver model with dedicated efficient solvers for each grid type. The communication between near-body and off-body solvers is accomplished through an automated overset grid assembly algorithm. The execution of the entire solution scheme is orchestrated through a high level object oriented python based computational platform. HELIOS has the capability for modeling the flow around a real wind turbine blade.

C. Mesoscale Microscale Coupling Interface (MMCI)

This module handles the interpolation of data between the mesoscale and microscale codes. MMCI can currently only handle one-way coupling between WRF, and the microscale codes. In this coupling approach, the mesoscale simulations are performed first. The data from the WRF simulations are fed to MMCI and this generates the boundary flow field information, and initial condition required for the CFD codes. The entire framework is setup using a high level object oriented python based computational platform.

One of the important requirements in the performance of the coupled LES is the interpolation of the SGS quantities between the different codes. This is necessary because the SGS quantities have much larger values on the coarse WRF grids compared to the fine microscale grids. This interpolation is performed by introducing a compatibility condition between the mesocale and microscale codes for the interpolation of the SGS variables. As both Flowyo and HELIOS are Eulerian CFD codes, the compatibility condition required for both these codes are the same. It is currently unclear on how to satisfy this compatibility condition in UWake. So, the current study uses the same compatibility condition with UWake as the other two CFD codes.

In the current study, the approach of Moeng et. al[23] is used to interpolate the viscosity and turbulent kinetic energy at the overset boundaries. This condition can be better understood by considering the budget of the turbulent kinetic energy, which can be symbolically written as follows

$$\text{Unsteady} + \text{Convection} = \text{Production} + \text{Dissipation} + \text{Diffusion} \tag{6}$$

In the above system, the convection, unsteady and diffusion terms are neglected in the overset regions and a balance between turbulent kinetic energy (TKE) production and dissipation is considered. This results in

$$(2\mu_t S_{ij}^d - \frac{2}{3}\rho k \delta_{ij})\frac{\partial U_i}{\partial x_j} = C_E \rho \frac{k^{3/2}}{\Delta} \tag{7}$$

where $\mu_t = C_k \rho \Delta \sqrt{k}$ is the dynamic viscosity, C_k is a model constant, Δ is the filer width, ρ is the fluid density, k is the SGS TKE, $S_{ij}^d = S_{ij} - S_{nn}/3$ is the deviatoric part of the strain tensor $S_{ij} =$

$1/2(\partial U_i/\partial x_j + \partial U_j/\partial x_i)$, and C_E is a model constant. If we substitute the expression for the dynamic viscosity in Eq. (7) and neglect the second-term on the left-hand side (negligible for low-speed flows), we obtain

$$k = 2\frac{C_k}{C_E}\Delta^2 S_{ij}^d \frac{\partial U_i}{\partial x_j} \tag{8}$$

If the effect of buoyancy (for convective boundary layers) or a non-linear model for SGS stress tensor is considered, an explicit solution still exists for the TKE. Once the value of TKE is calculated at the overset boundaries from the interpolated velocities, the dynamic viscosity can be obtained from it. The above condition is implicitly satisfied when the Smagorinsky model is used while it has to be explicitly satisfied for the other models. It should be noted that the grid points in the overset region are available for the solver through iblanking and no additional effort is required to explicitly calculate the turbulent viscosity in the overset regions.

D. Simulation Setup

The coupled numerical simulations are performed in five stages, as outlined below:

1. Generate the grid and perform the WRF simulations.
2. Generate the grid for the microscale CFD solver.
3. Set-up the MMCI interpolation information.
4. Initialize the microscale CFD solver from WRF flow field data.
5. Run the CFD simulations.

The first step is the same for all the three solvers and can be performed independently. The details of performing LES using WRF can be found in Mirocha et. al[11] and will not be repeated here. All the WRF-LES simulations in the current study used a numerical grid which satisfies the condition: $dx = dy = 4dz$. After, the WRF simulations are completed, the one-way coupling is implemented differently for each solver and will be discussed separately. It should be noted that MMCI is able to handle all the solvers within the same framework.

1. UWake

For simulations performed using UWake, the only requirement is that the freestream component of the markers are obtained from WRF data. This is accomplished using a straight forward trilinear interpolation.

2. Flowyo

The domain setup for the coupled simulations using Flowyo is shown in Figs. 6a-c. The outer box in Fig. 6 is a schematic representation of the WRF domain while the inner shaded box represents the CFD domain (referred as off-body domain). The off-body domain uses a single-block structured grid with grid refinement in the terrain normal direction, if required. The overset grid boundaries at the interface between the off-body domain and WRF domain is shown in Fig. 6b for a single grid line. It is not required to have only one line in the overset region. Multiple grid points can be used and the MMCI module takes care of calculation of the velocities and SGS quantities at all these locations. The WRF flow field information is interpolated to the off-body domain using the MMCI module while the turbulent viscosity in the CFD domain is calculated using Eq. (8). The same procedure is used at the boundaries between the near-body and off-body domain. The interpolation information at the overset grid boundaries are calculated dynamically to avoid significant overhead associated with storage of the WRF data in the memory for the entire time span. This setup is sufficient for performing wind resource estimation studies. It should be noted that for complex terrains, curvilinear single-block structured grids are used and the MMCI module can account for the curvature in the terrain. Fluid Structure Interaction capability can also be added by incorporating the structural module to the CFD solver.[24] For modeling a wind turbine using actuator disc or actuator line, cylindrical structured grids (referred as near-body domain) are overset inside the off-body domain. One such grid is used for each turbine. This automates the grid generation process and makes it easier to add any number of turbines

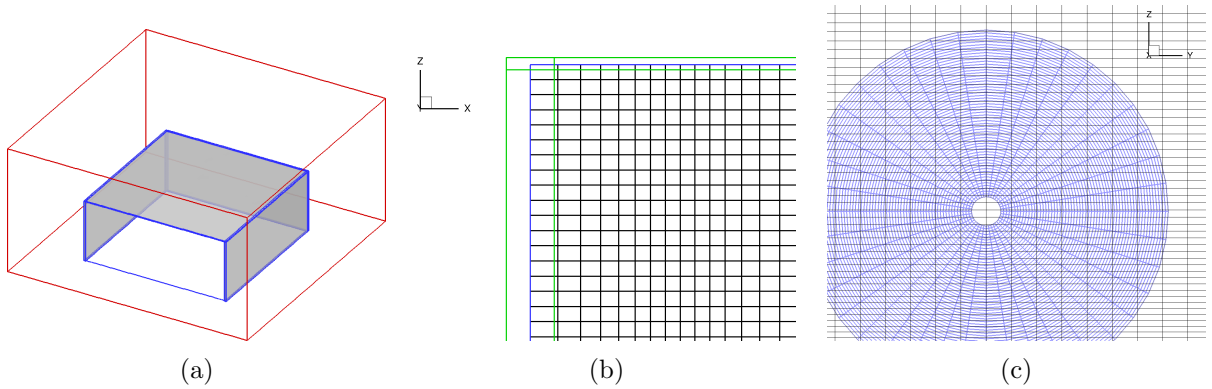

Figure 6. Mesoscale-Microsale interfacer: (a) Schematic of the WRF domain (shown in red), and off-body CFD domain (shown in blue). The inner shaded region indicates the boundaries at which data is interpolated from the WRF to the off-body domain. (b) Schematic of the overset assembly at the top and inflow boundaries. The CFD boundary (shown in blue, black lines represent the CFD grid) is overset within WRF cell centers (shown in green). and (c) Schematic of the near-body actuator grid (shown in blue) overset within the off-body grid (shown in black) in Flowyo.

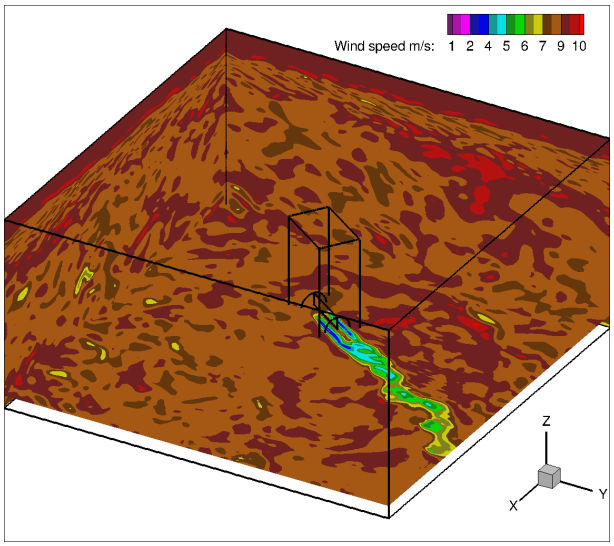

Figure 7. Setup of the coupled simulation in Flowyo with a single wind turbine.

in the CFD domain in a straight forward way without the need for multiple levels of grid refinement.[25] The overlapping regions of the off-body and near-body grids are shown in Fig. 6c for a single turbine grid. Once the grids for all the wind turbines have been assembled, the WRF flow field information is used to initialize both the domains. In this way, the simulations can be started using realistic initial conditions. The simulations are performed after the initial conditions have been generated. A sample flow field for a coupled simulation with a single wind turbine is shown in Fig. 7. It should be noted that the time step of simulation in Flowyo is much smaller than the WRF simulations. A weighted linear interpolation is used for interpolation of boundary data from WRF to the CFD domain at time steps which do not coincide with the WRF data.

3. HELIOS

HELIOS mesh system consists of body conforming (termed near-body meshes) that are overlapped by a system of nested Cartesian grids of incremental resolution. The Sexbierum site wind turbine, which was previous analyzed by the authors[9] in steady flow conditions, was chosen as the turbine model for illustration of the setup. Near-body meshes that conform to this three bladed turbine consisted of 2.15 million grid points

with stretched cells at the surface to provide enough resolution to match the viscous sub-layer requirement for RANS simulations. The off-body grid system is capable of dynamic feature based adaptation and hence grew from about 6 million grid points in the beginning to 250 million grid points in 50000 steps of unsteady simulation (equivalent to 60 seconds of physical time).

In Figure 8(a) we show the near and off-body grid systems utilized by HELIOS. The modular MMCI developed as part of this work is applied in the same manner as in the Flowyo simulation. The outer boundaries of HELIOS meshes are setup such that they are overlapped by the extracted WRF boundary representation. Consequently, weighted interpolation is performed to project velocity from WRF on to the HELIOS outer boundaries. In Figure 8(b) we show flow visualization obtained from unsteady simulations. The local velocity field from meso-scale simulations can be observed to induce unsteady perturbations and cause meandering and break down of the vortex wake emanating from the turbine.

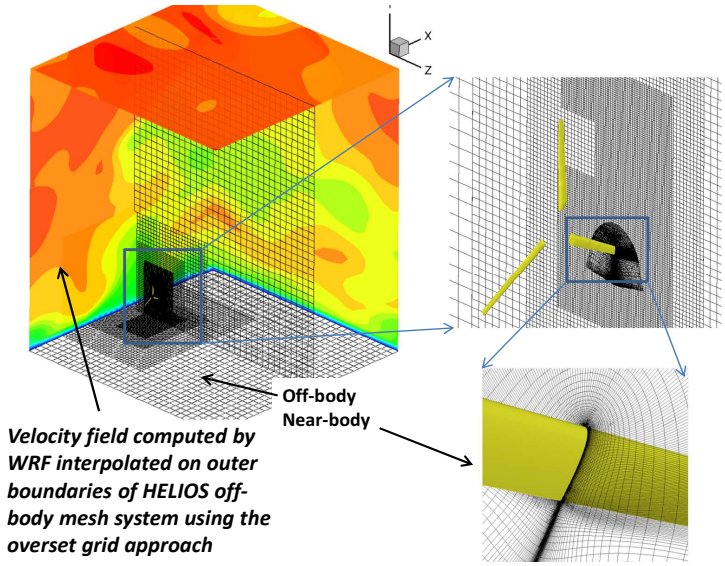

(a) helios mesh system

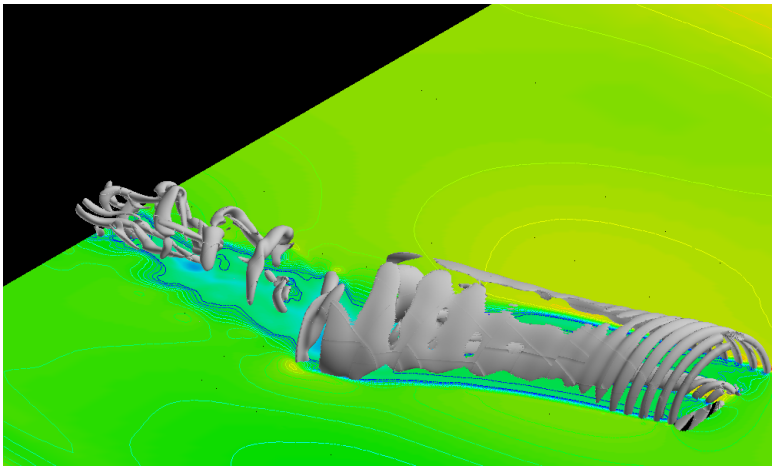

(b) Wake response to turbulent inflow

Figure 8. (a) HELIOS mesh system consisting of near- and off-body meshes. Near-body meshes are body-conforming and provide and effective method for resolving the viscous sub-layer near the moving wind turbine walls (wall spacing = $1\mu m$). Off-body meshes provide nesting and adaptation capabilities and effective scaling of the resolution to match grid resolution of WRF data (outer grid spacing = $10m$). (b) Iso-vorticity contours overlaid with velocity field after 50000 steps of unsteady simulation: velocity fields on plane parallel to the ground and passing through the turbine hub are shown.

III. Initial Results and Discussion

The initial results obtained from the coupled simulation are shown in the current section for UWake, Flowyo and HELIOS. As the coupling with Cgins is currently under development, we show initial results for a single turbine in uniform inflow. The final version of the paper will include the coupled simulation results for Cgins.

A. UWake

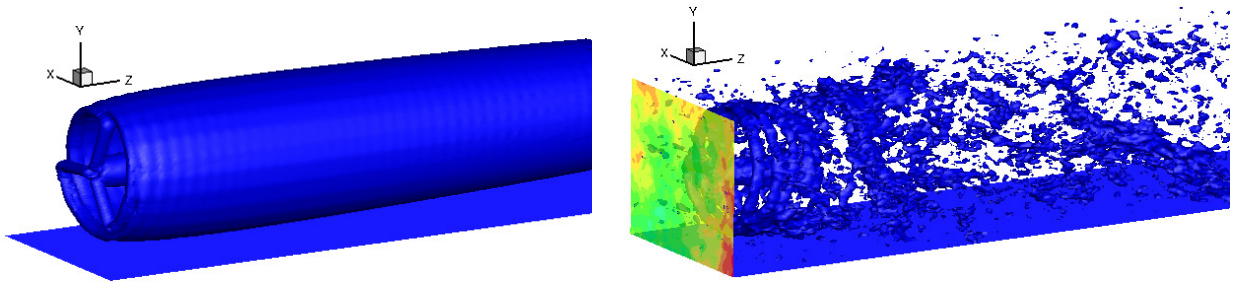

(a) (b)

Figure 9. Iso-vorticity contours for the Sexbierum turbine at 8 m/s for a (a) steady and (b) turbulent inflow.

The wind turbine blade used in the experimental Sexbierum wind farm[26] was chosen for this investigation. The WRF simulations were performed using a equal horizontal mesh resolution of 16 m and a vertical mesh resolution of 4 m was used. The grid was uniform in all the three directions. The domain size was taken to be 2048 m in the horizontal directions and 1024 m in the vertical direction. The simulations were driven using a uniform geostrophic wind: $(u_g, v_g) = (10, 0)$ m/s at a latitude of 45^o. Periodic boundary conditions were employed along the streamwise and spanwise directions. At the lower vertical boundary, the SGS stresses were calculated using the wall-function approach with a roughness length $z_o = 0.1$ m. A free slip boundary condition was employed at the top of the domain. The heat flux at the surface was specified to be zero as the simulations were performed for a neutral boundary layer. The comparison between the turbine in uniform inflow and turbulent inflow are shown in Fig 9. The turbulent inflow has been enhanced by the addition of the synthetic inflow. It can be seen that the addition of the fluctuations to turbulent inflow causes the breakdown of the vortex structures in the wake which the uniform inflow case is not able to capture.

An operational off-shore wind farm operated by Vattenfall Vindkraft AB is also simulated using the coupled approach. The installed wind turbines in the farm were 48 Siemens SWT-2.3-93 three-bladed, upwind, horizontal-axis turbines. As the wind turbine blade information was not available, an approximate method proposed by Churchfield[25] was used for generation of the aerodynamic information of the wind turbine blade, required for actuator models. The WRF simulations were performed on a domain size of $4096 \times 4096 \times 1024$ m with a horizontal grid resolution of 16 m and a vertical grid resolution of 4 m. The mean wind speed and turbulent intensity profiles were matched closely to the existing conditions at the wind farm. The hub-height wind speed for simulations performed using uniform inflow, WRF inflow, and synthetic inflow using inflow model in shown in Fig 10.The improved resolution of the turbulent structures in the flow is clearly evident.

B. Flowyo

Similar to UWake simulations, results obtained from Flowyo simulations are shown for both single turbine and wind farm. Lillgrud wind turbine blade and wind farm is used for both these simulations, respectively. The comparison of the turbine power for the uniform, turbulent inflow, and turbulent inflow with added fluctuations is shown in Fig 11. The average power production from all the simulations are close to each other. However, the mean values do not give any information of the turbulence in the wind farm. Contours of instantaneous wind speed at the hub-height are shown for all the three cases in Fig 12. There is a clear difference in the propagation and recovery of the wake. In the uniform inflow case, the wake propagates for large distances downstream without recovery. The turbulent inflow case shows that the wake recovers faster while this happens much faster for the turbulent inflow with added fluctuations. These results clearly

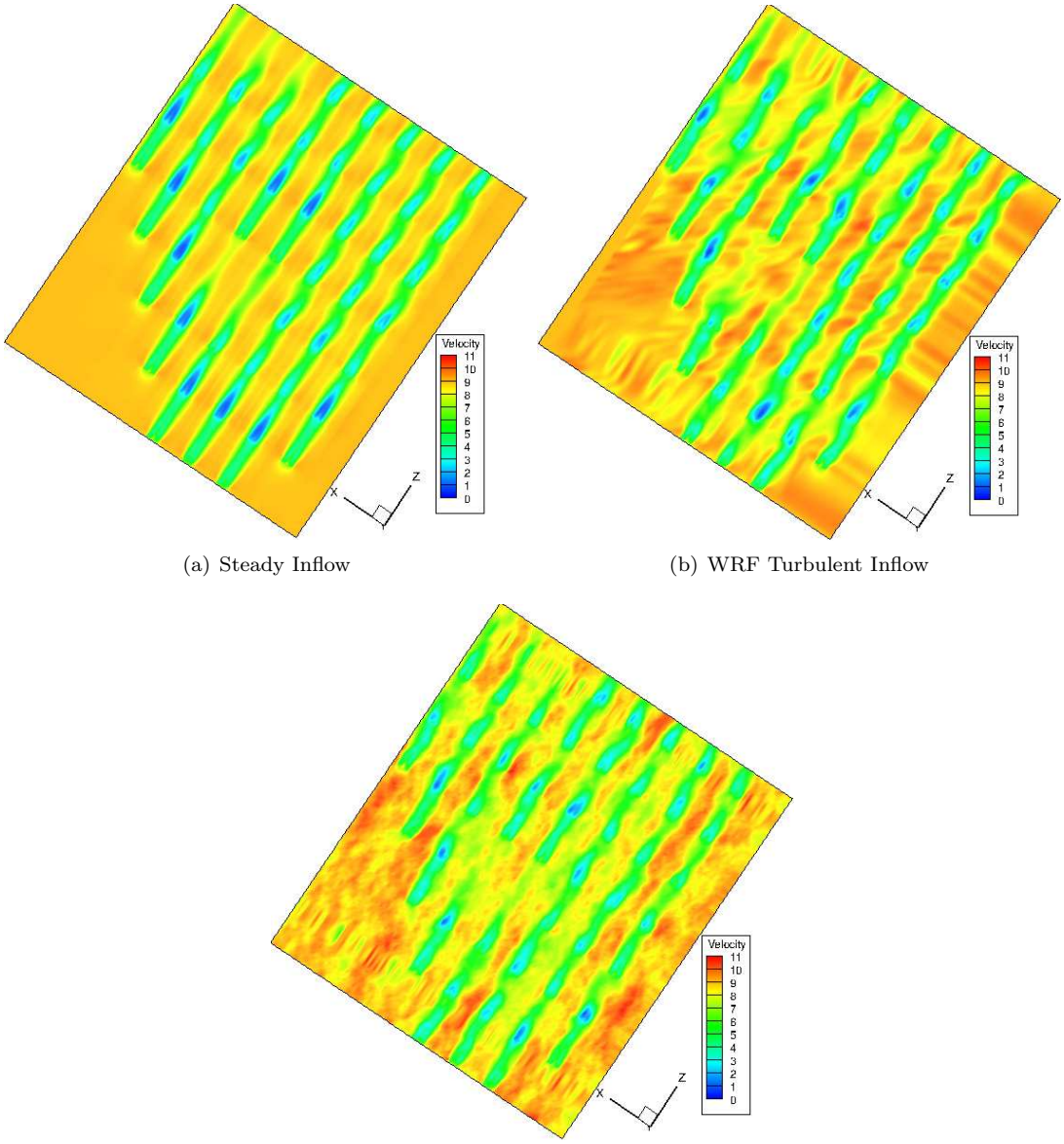

(a) Steady Inflow

(b) WRF Turbulent Inflow

(c) Mann Turbulent Inflow

Figure 10. Hub height velocity contours at $8.5\ m\ s^{-1}$ **for UWAKE with a) uniform inflow, b) WRF turbulent inflow and c) synthetic inflow using inflow model**

suggest that for a wind farm with multiple turbine scenario with multiple wake atmospheric interaction, there will be significant difference in the instantaneous power production between turbines operating in uniform and turbulent inflow. In particular, the mean power produced by downstream turbines in the wake of the upstream turbine, will be much higher for the turbulent inflow case compared to the uniform inflow. Similar to UWake simulations, the comparison of the wind speed at hub-height is shown in Fig 13 for all the three cases for the lillgrund wind farm. Significant differences are seen and will be evaluated in detail in the final paper.

C. Cgins

The coupling between the mesoscale and Cgins is still under development. Currently, we can perform simulations using actuator disk parametrization of the wind turbine in uniform flow. Figure 14 shows the

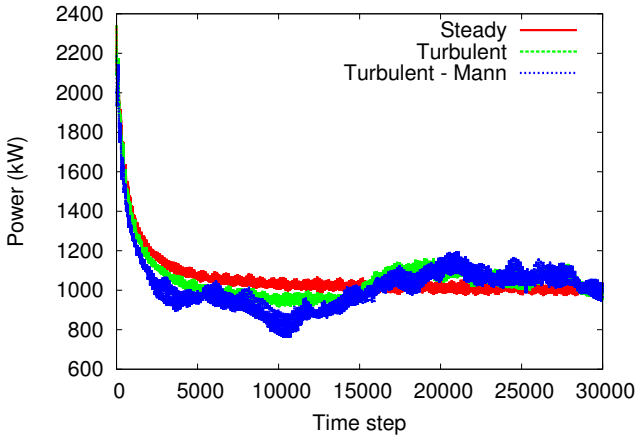

Figure 11. Comparison of the turbine power for uniform, WRF turbulent inflow and synthetic inflow using actuator line model. The results are shown for every 50 time steps.

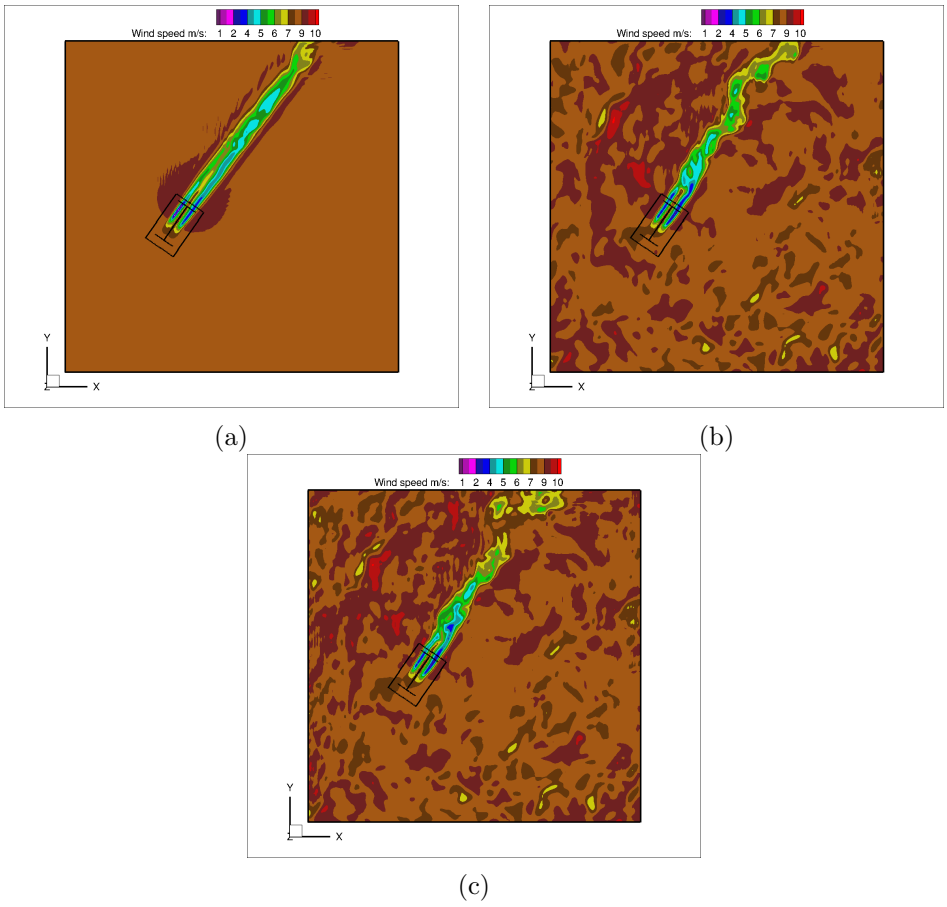

Figure 12. Instantaneous wind speed at hub-height for single turbine scenario: (a) uniform inflow, (b) WRF turbulent inflow and (c) synthetic inflow using inflow model.

normalized streamwise velocity behind a NREL phase VI wind turbine that was simulated using Cgins. It can be seen that the turbine wake region is clearly captured by the simulations. The final paper will include results from Cgins for wind turbine in turbulent inflow.

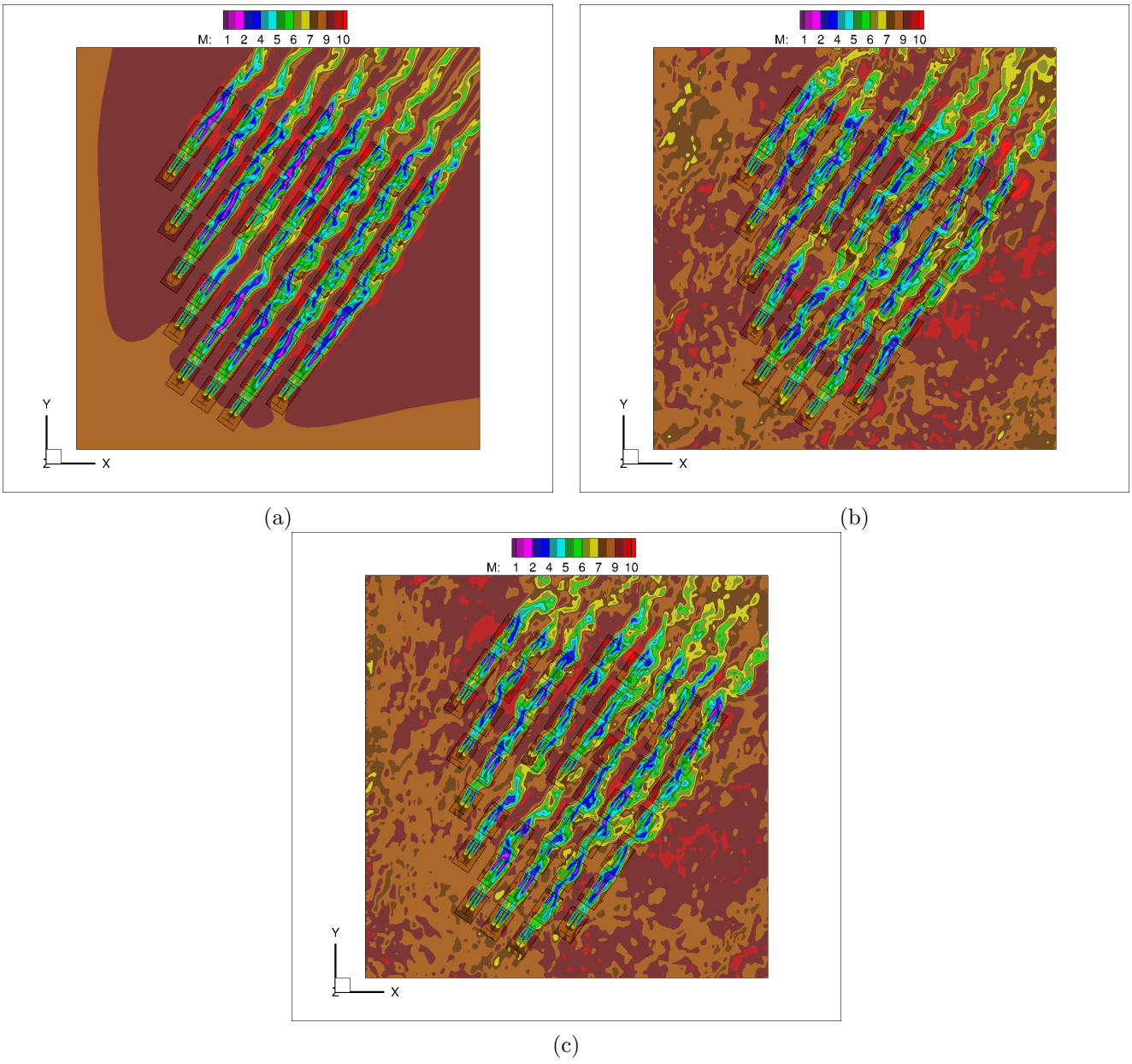

Figure 13. Instantaneous wind speed at hub-height for the wind farm: (a) uniform inflow, (b) WRF turbulent inflow and (c) synthetic inflow using inflow model.

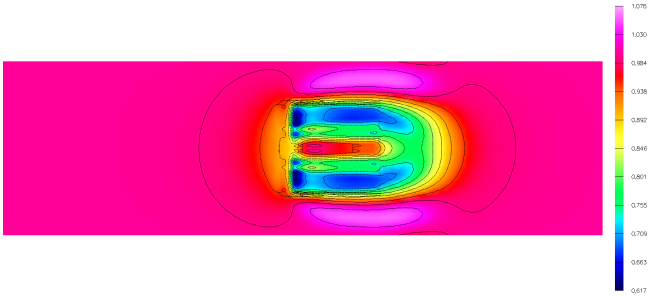

Figure 14. Streamwise velocity in a plane cut along the axis of the turbine. Simulations were performed using Cgins with actuator disc model of the wind turbine.

D. HELIOS

HELIOS simulations were conducted for the WPS-30 turbine from the Sexbierum experimental site. The MMCI module was used to include the effects of the atmospheric boundary layer using the strategy described in the methodology section. In Figure 15, the thrust and power variation for the WRF/Helios (Meso-scale/micro-scale simulation) is compared with measured power and stand-alone Helios computations (uniform inflow). The unsteady variations in power and thrust caused by the turbulent inflow conditions is clearly evident from these figures. Note that the mean hub-height velocity could not be exactly matched to the uniform inflow values of 8 m/s because of constraints in adjusting the geostrophic wind and roughness length in Meso-scale WRF simulations. The offset in mean power and thrust notable in the figures are because of the small difference in the mean wind speed. Nonetheless, these results provide proof-of-concept of the integrated Meso-scale/Micro-scale simulation capability developed as part of this work. To further substantiate the effects of turbulent inflow, flow visualizations (iso-surfaces of vorticity overlaid on contours of velocity magnitude) are shown in Figure 16. Meandering of the vortex wake and eventual breakdown are observed in the flow visualizations. Vortex breakdown is observed to occur between 1.5 and 2.5 diameter distance from the turbine. In uniform inflow (not shown here), the vortex wake persists to much longer distance of about 5 diameters before beginning to breakdown. It is expected that the vortex breakdown will be strongly correlated with the turbulence intensity of the inflow. The capability developed herein provides enabling technology for analyzing and characterizing such effects.

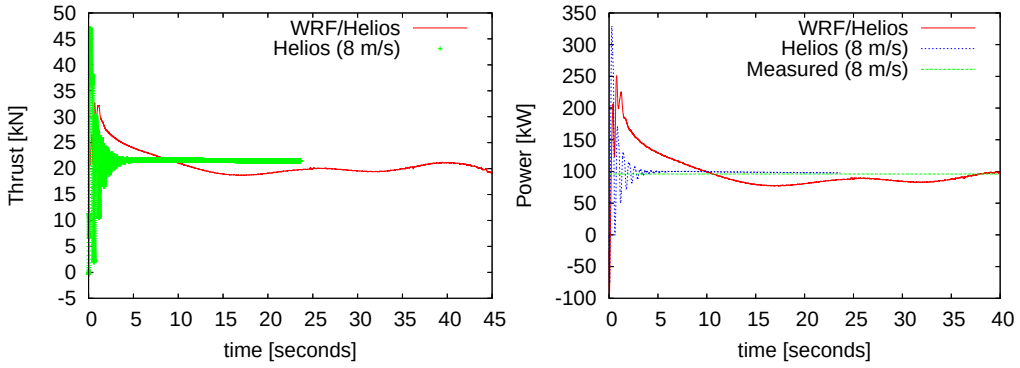

(a) Thrust variation (b) Power variation

Figure 15. Thrust and power variation obtained from coupled WRF/Helios simulations compared with stand alone Helios computations

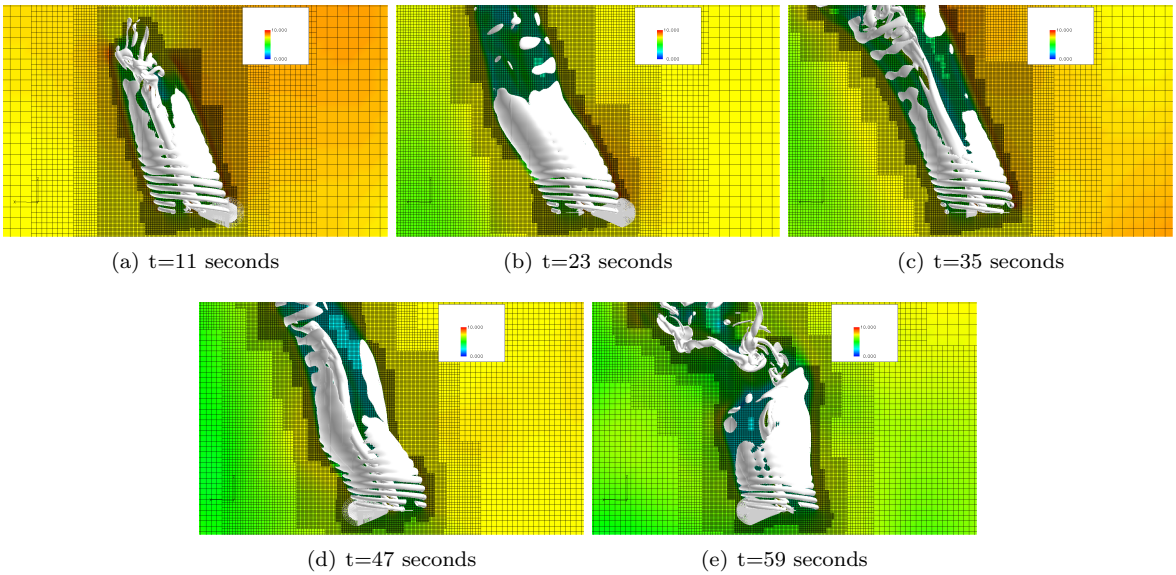

(a) t=11 seconds (b) t=23 seconds (c) t=35 seconds

(d) t=47 seconds (e) t=59 seconds

Figure 16. Iso surfaces of vorticity ($\omega = 0.003$) overlaid with velocity contours. Grid systems are also overlaid on the flow visualizations to show the efficacy of solution based AMR.

IV. Future Work

The setup which has been demonstrated in the abstract will be applied to a real site in which wind speed measurements will be made from a met tower and Windcube lidar. Sample results are shown in Fig 17 . The wind speed measurements will be used to construct the precursor WRF simulations and the analysis which has been demonstrated in the abstract will be repeated for single and multiple turbines using the four different microscale solvers for different turbulent intensities, shear distributions and stability conditions which would match the existing conditions at the site.

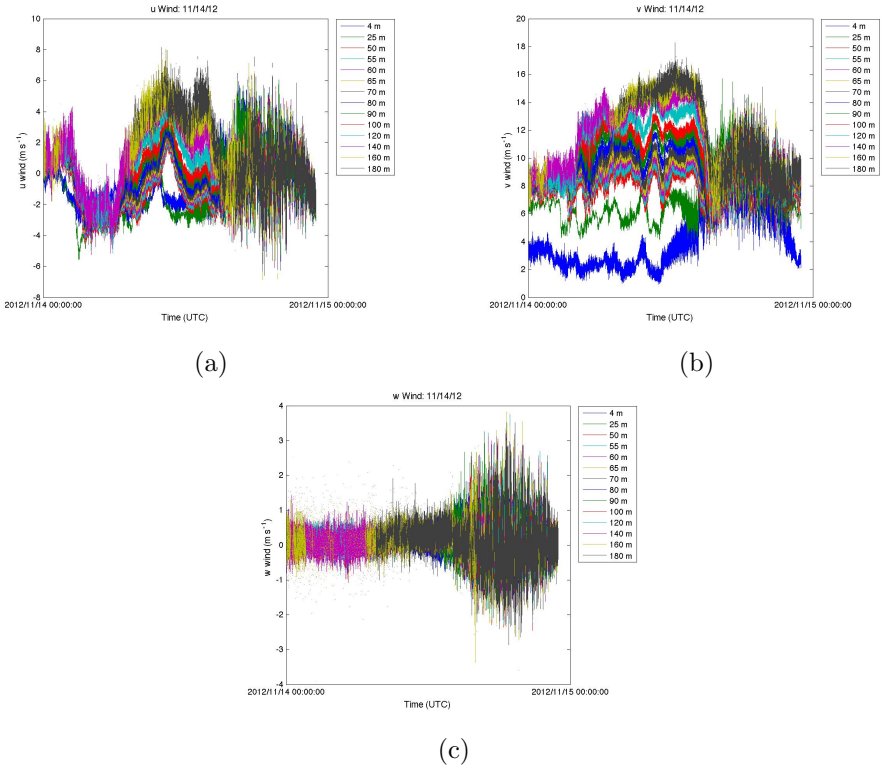

Figure 17. Measured wind speeds using met tower and WindCube lidar:(a) x-component inflow, (b) y-component and (c) z-component.

V. Acknowledgments

The first four authors gratefully acknowledge Lawrence Livermore National Labs for continued support of this work. The authors would also like to thank Dr. Bob Meakin who directs the DoD CREATE/AV program and Dr. Roger Strawn at the Army Aeroflightdynamics directorate at NASA Ames for providing access to the use of HELIOS software framework.

Prepared by LLNL under Contract DE-AC52-07NA27344.

References

[1]Focken, U., Lange, M., Mönnich, K., Waldl, H. P., Beyer, H. G., and Luig, A., "Short-term prediction of the aggregated power output of wind farmsa statistical analysis of the reduction of the prediction error by spatial smoothing effects," *Journal of Wind Engineering and Industrial Aerodynamics*, Vol. 90, No. 3, 2002, pp. 231–246.

[2]Yu, W., Benoit, R., Girard, C., Glazer, A., Lemarquis, D., Salmon, J. R., and Pinard, J. P., "Wind Energy Simulation Toolkit (WEST): A wind mapping system for use by the WindEnergy Industry," *Wind Engineering*, Vol. 30, No. 1, 2006, pp. 15–33.

[3]Zajaczkowski, F. J., Haupt, S. E., and Schmehl, K. J., "A preliminary study of assimilating numerical weather prediction data into computational fluid dynamics models for wind prediction," *Journal of Wind Engineering and Industrial Aerodynamics*, Vol. 99, No. 4, 2011, pp. 320–329.

[4]Park, J., Basu, S., and Manuel, L., "Large-eddy simulation of stable boundary layer turbulence and estimation of associated wind turbine loads," *Wind Energy*, Vol. in press, 2013, pp. 1 – 26.

[5]Mann, J., "The spatial structure of neutral atmospheric surface-layer turbulence," *Journal of Fluid Mechanics*, Vol. 273, 1994, pp. 141–168.

[6]Skamarock, W. C. and Klemp, J. B., "A time-split nonhydrostatic atmospheric model for weather research and forecasting applications," *J. Comp. Phys.*, Vol. 227, No. 7, 2008, pp. 3465–3485.

[7]Henshaw, W. D., Kreiss, H.-O., and Reyna, L. G., "A fourth-order-accurate difference approximation for the incompressible Navier-Stokes equations," *Computers & fluids*, Vol. 23, No. 4, 1994, pp. 575–593.

[8]Gundling, C., Roget, B., and Sitaraman, J., "Prediction of Wind Turbine Performance And Wake Losses Using Analysis Methods Of Incremental Complexity," *AIAA Aerospace Sciences Meeting and Exhibit*, Orlando, FL, January 2011, pp. AIAA Paper 2011–0458.

[9]Gundling, C., Roget, B., Sitaraman, J., and Rai, R., "Comparison of Wind Turbine Wakes in Steady and Turbulent Inflow," *50th AIAA Aerospace Sciences Meeting*, Nashville, TN, January 2012, pp. AIAA Paper 2012–0899.

[10]Kosovic, B., "Subgrid-scale modelling for the large-eddy simulation of high-Reynolds-number boundary layers," *Journal of Fluid Mechanics*, Vol. 336, No. 1, 1997, pp. 151–182.

[11]Mirocha, J. D., Lundquist, J. K., and Kosovic, B., "Implementation of a Nonlinear Subfilter Turbulence Stress Model for Large-Eddy Simulation in the Advanced Research WRF Model," *Mon. Wea. Review*, Vol. 138, No. 11, 2010, pp. 4212–4228.

[12]Rai, R., Gopalan, H., Naughton, J. W., and Heinz, S., "A Study of the Sensitivity of Wind Turbine Response to Inflow Temporal and Spatial Resolution," *50th AIAA Aerospace Sciences Meeting and Exhibit*, Nashville, TN, January 2012, pp. AIAA Paper 2012–0819.

[13]Bhagwat, M. J. and Leishman, J. G., "Stability, consistency and convergence of time-marching free-vortex rotor wake algorithms," *Journal of the American Helicopter Society*, Vol. 46, No. 1, 2001, pp. 59–71.

[14]Duf, Z. and Selig, M. S., "A 3-D Stall-Delay Model for Horizontal Axis Wind Turbine Performance Prediction," *A collection of the 1998 ASME Wind Energy Symposium technical papers: at the 37th AIAA Aerospace Sciences Meeting and Exhibit, Reno, NV, January 12-15, 1998*, American Institute of Aeronautics and Astronautics, 1998, p. 9.

[15]Van Leer, B., "Towards the ultimate conservative difference scheme. V. A second-order sequel to Godunov's method," *Journal of computational Physics*, Vol. 32, No. 1, 1979, pp. 101–136.

[16]Liu, X., Osher, S., and Chan, T., "Weighted essentially non-oscillatory schemes," *Journal of Computational Physics*, Vol. 115, No. 1, 1994, pp. 200–212.

[17]Yoon, S. and Jameson, A., "Lower-upper symmetric-Gauss-Seidel method for the Euler and Navier-Stokes equations," *AIAA journal*, Vol. 26, No. 9, 1988, pp. 1025–1026.

[18]Smagorinsky, J., "General circulation experiments with the primitive equations," *Monthly weather review*, Vol. 91, No. 3, 1963, pp. 99–164.

[19]Deardorff, J., "Three-dimensional numerical study of the height and mean structure of a heated planetary boundary layer," *Boundary-Layer Meteorology*, Vol. 7, No. 1, 1974, pp. 81–106.

[20]Nicoud, F. and Ducros, F., "Subgrid-scale stress modelling based on the square of the velocity gradient tensor," *Flow, Turbulence and Combustion*, Vol. 62, No. 3, 1999, pp. 183–200.

[21]Spalart, P., Jou, W., Strelets, M., and Allmaras, S., "Comments on the feasibility of LES for wings, and on a hybrid RANS/LES approach," *1st AFOSR Intl. Conf. on DNS/LES*, Columbus: Greyden Press, Ruston, LA, USA, Aug. 4-8 1997, pp. 4–8.

[22]Spalart, P. R., Deck, S., Shur, M. L., Squires, K. D., Strelets, M. K., and Travin, A., "A new version of detached-eddy simulation, resistant to ambiguous grid densities," *Theoretical and Computational Fluid Dynamics*, Vol. 20, No. 3, 2006, pp. 181–195.

[23]Moeng, C., Dudhia, J., Klemp, J., and Sullivan, P., "Examining two-way grid nesting for large eddy simulation of the PBL using the WRF model," *Monthly weather review*, Vol. 135, No. 6, 2007, pp. 2295–2311.

[24]Masarati, P. and Sitaraman, J., "Coupled CFD/Multibody Analysis of NREL Unsteady Aerodynamic Experiment Phase VI Rotor," *AIAA Aerospace Sciences Meeting and Exhibit*, Orlando, FL, January 2011, pp. AIAA Paper 2011–153.

[25]Churchfield, M. J., S. Lee, P. J. M., Martinez, L. A., Leonardi, S., Vijayakumar, G., and Brasseur, J. G., "Large-Eddy Simulations of Wind-Plant Aerodynamics," *50th AIAA Aerospace Sciences Meeting and Exhibit*, Nashville, TN, January 2012, pp. AIAA Paper 2012–537.

[26]Cleijne, J. W., "Results of Sexbierum Wind Farm; single wake measurements," Tech. Rep. 93-082, 112324-22420, TNO-report, 1993.